Materials Research Letters

ISSN: (Print) 2166-3831 (Online) Journal homepage: http://www.tandfonline.com/loi/tmrl20

Silver-rich clusters in nanoporous gold

Tobias Krekeler, Anastasia V. Straßer, Matthias Graf, Ke Wang, Christian Hartig, Martin Ritter & Jörg Weissmüller

To cite this article: Tobias Krekeler, Anastasia V. Straßer, Matthias Graf, Ke Wang, Christian Hartig, Martin Ritter & Jörg Weissmüller (2017) Silver-rich clusters in nanoporous gold, Materials Research Letters, 5:5, 314-321, DOI: 10.1080/21663831.2016.1276485

To link to this article: https://doi.org/10.1080/21663831.2016.1276485

Published online: 17 Jan 2017.

MATER. RES. LETT., 2017
VOL. 5, NO. 5, 314–321
http://dx.doi.org/10.1080/21663831.2016.1276485

MATERIALS RESEARCH LETTERS
Taylor & Francis
Taylor & Francis Group

ORIGINAL REPORT

OPEN ACCESS

Silver-rich clusters in nanoporous gold

Tobias Krekeler[a], Anastasia V. Straßer[b], Matthias Graf[b], Ke Wang[b], Christian Hartig[b], Martin Ritter[a] and Jörg Weissmüller [b,c]

[a]Electron Microscopy Unit, Hamburg University of Technology, Hamburg, Germany; [b]Institute of Materials Physics and Technology, Hamburg University of Technology, Hamburg, Germany; [c]Institute of Materials Research, Materials Mechanics, Helmholtz-Zentrum Geesthacht, Geesthacht, Germany

ABSTRACT

High-resolution elemental mapping in a transmission electron microscope shows that the residual silver in dealloying-made nanoporous gold (NPG) is aggregated in nanoscale clusters. Kinetic Monte Carlo simulation confirms that these regions are buried relics of the master alloy that have never been exposed to corrosion. The surface of as-dealloyed NPG is covered by at least one atomic monolayer of nearly pure gold. The preferential location of silver in the bulk is relevant when interfaces control the material's function, as in catalysis and sensing. Annealing in air homogenizes the alloy by surface diffusion.

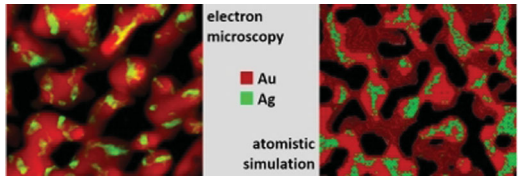

IMPACT STATEMENT

The residual silver which is typically found in nanoporous gold made by dealloying is localized in clusters that are relics of the original master alloy which have evaded corrosion.

ARTICLE HISTORY
Received 5 December 2016

KEYWORDS
Dealloying; nanoporous gold; elemental mapping; electron microscopy; kinetic Monte Carlo simulation

1. Introduction

Nanoporous gold (NPG) made by dealloying takes the form of a network of nanoscale struts or 'ligaments' that can be prepared in macroscopic dimensions yet with characteristic ligament sizes, L, reaching down to the lower nanometer scale [1]. The uniformity of the network microstructure, along with the option of reproducibly selecting L between few nm and microns, makes the material an attractive model system for studies of size and interface effects in nanomaterials. This is exemplified by many recent studies of NPG in the field of small-scale plasticity and elasticity [2–9]. Interest is also on the use of NPG as a functional material, for instance in the fields of actuation or sensing [10–14], energy storage [15], optics [16–18] and microfluidics [19]. Particularly intriguing is the high activity of NPG as a heterogeneous catalyst [16,20,21], since classic observations of Au as a catalyst focus on oxide-supported nanoparticles.

The standard approach for making NPG is by dealloying, that is, by selectively dissolving Ag from an Ag–Au solid solution via controlled corrosion. As the master alloy is uniform, the nanoscale structure forms by the interplay of the elementary processes at the corrosion front, Ag dissolution and Au surface diffusion [1,22]. Samples of NPG typically contain in the order of 5 at.-% 'residual' Ag. The role of the silver for the materials performance is emphasized in the literature. Its impact on the elastic properties has been highlighted [23], yet details of the elastic behavior of NPG remain the subject of debate [9]. Silver also affects the stacking fault energy and, thereby, the nature (full or partial) of the lattice dislocations that carry the plastic deformation and that decide which of the conflicting scenarios applies: small-scale strengthening by dislocation starvation [24,25] or dislocation interaction and Taylor work hardening [26,27]. Surface-enhanced Raman scattering

CONTACT Jörg Weissmüller weissmueller@tuhh.de Institute of Materials Physics and Technology, Hamburg University of Technology, Eißendorfer Straße 42, 21073 Hamburg, Germany

(SERS) of NPG is also significantly affected by the residual Ag [11]. Furthermore, the role of residual Ag for the catalytic properties of NPG is under debate [28–33].

In each of the above instances, the *spatial distribution* of the residual Ag can be decisive. Here, we discuss this issue based on high-resolution elemental mapping in a transmission electron microscope, supported by kinetic Monte Carlo (KMC) simulation of dealloying. We find that a major part of the residual Ag in as-dealloyed NPG is aggregated in buried silver-rich clusters. We point out that this finding is, in fact, a natural consequence of the standard model of microstructure evolution during dealloying.

2. Methods

Ag and Au, at ratio $Ag_{75}Au_{25}$ (subscripts: at.-%), were alloyed by arc-melting, sealed in fused silica and annealed for 100 h at 850 °C for homogenization. Wire drawing and cutting to mm-size dimensions were followed by a recovery anneal in vacuum, 3 h at 650 °C. Dealloying of the samples for transmission electron microscopy (TEM) followed the protocol of Wang et al. [34] (denoted as route A) using 1 M $HClO_4$ at potential 0.75 V versus a Ag/AgCl pseudo-reference electrode in the same solution. After the current decreased to below 10 µA, the applied potential was held at 0.85 V for 3 h for further Ag removal. An alternative dealloying method (route B) followed the protocol of Wittstock et al. [28], with corrosion in 5 M HNO_3 at potential 0.06 V versus a Pt pseudo-reference electrode. Durations varied between 6 and 24 h.

Samples for TEM were vacuum impregnated with epoxy resin and cured (20 min at 60 °C) as in [34]. Electron-transparent slices were cut with an EM UC7 ultramicrotome (Leica). After trimming, the block face with a Trim 45 knife (Diatome) to an area of roughly 1 mm^2, 30–170 nm thin slices were cut using an Ultra 35 knife at 0.6 mm/s in order to minimize stress. Slices were then transferred to a 400 mesh copper folding grid.

An FEI Talos F200X transmission electron microscope equipped with a high brightness Schottky-FEG (X-FEG) and a four-quadrant SDD-EDS System with a solid angle of 0.9 srad was used for high-angle annular dark-field (HAADF) imaging and energy-dispersive x-ray spectroscopy (EDS) analysis. Spectrum images (SI) for quantification of Ag and Au were acquired using a probe current of 0.4 nA and a dwell time of 20 µs per pixel. Total acquisition time was 12 h for an SI of 512 × 512 pixels, 0.7 nm in size, resulting in a horizontal field of view of 384 nm. Esprit 1.9 (Bruker) was used for data acquisition and quantification.

The tilt series for tomographic reconstruction was composed of 66 SI (from +65° to −65° with a spacing of 2°) of a 70 nm ultramicrotomy slice, acquired using a tomography specimen holder (Fischione 2020). The probe current was 0.8 nA and the dwell time 20 µs per pixel. The resolution of the SI was 256 × 256 pixels with a pixel size of 1.5 nm, resulting in a horizontal field of view of 384 nm. The SI were denoised via principal component analysis on the whole spectrum image data set using Hyperspy [35]. For volume reconstruction and visualization, Inspect3D 4.1.1 (FEI) and Avizo 9.0.0 (FEI) were used, respectively.

Our KMC simulation of dealloying is an implementation of the algorithm by Erlebacher [22], using the identical materials parameters and rate terms. The simulation tracks the evolution of a random binary solution of Ag and Au on a face-centered cubic lattice, allowing for two elementary events in the ensemble of surface atoms, while all other atoms are inert. Event 1 models surface diffusion by the nearest-neighbor jump of an Au or Ag atom, with the diffusion rate $k_{\mathrm{diff}} = \nu_{\mathrm{D}} \exp(nE_{\mathrm{b}}/k_{\mathrm{B}}T)$. The symbols denote: ν_{D}—Debye frequency ($10^{13} s^{-1}$), n—initial site coordination, E_{b}—bond energy (here −0.15 eV), T—temperature, and k_{B}—Boltzmann constant. Event 2 models dissolution by the removal of an Ag atom, with the rate $k_{\mathrm{diss}} = \nu_{\mathrm{E}} \exp((nE_{\mathrm{b}} + e\Phi)/k_{\mathrm{B}}T)$. The prefactor, $\nu_{\mathrm{E}} = 10^4\ s^{-1}$, is related to the exchange current density for Ag dissolution, e denotes the elementary charge and Φ parameterizes the electrode potential, see [22]. Our implementation uses the Hoshen–Kopelman cluster method [36] for identifying atoms with at least one neighbor from the largest vacancy cluster, which form the (open pore) surface ensemble. Dissolution is restricted to surface atoms with a sufficiently open neighborhood, which requires adjacent planar vacancy clusters with at least three vacancies. Furthermore, diffusion is restricted to target sites with at least three neighbor atoms. In particular, this prevents regular Schwöbel jumps.

The simulation was performed on a cuboid sample of initial composition $Ag_{75}Au_{25}$, 100 × 100 atoms in lateral size and 90 {111} layers thick, using periodic boundary conditions in the plane. We found that setting Φ = 1.14 V resulted in sufficiently fast kinetics to allow following the corrosion through its initial stages and a significant coarsening regime. The open-source software OVITO [37] was used for visualization.

3. Results and discussion

Our TEM study focused on samples made by route A, which is adopted by many studies requiring NPG with optimum mechanical behavior. Supplementary data came from samples made by route B, which affords

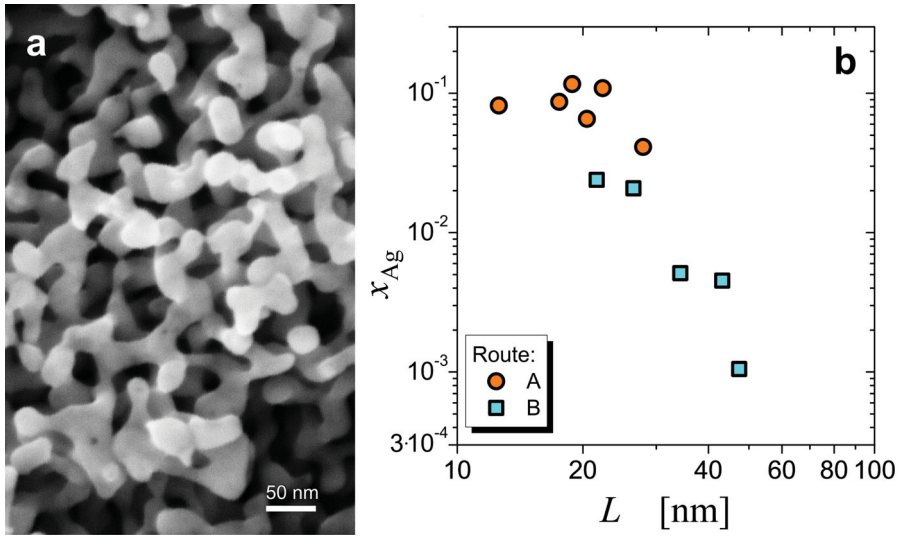

Figure 1. NPG: microstructure and residual silver fraction. (a) Scanning electron micrograph of the cleavage surface of a representative as-dealloyed sample (route A), showing the characteristic three-dimensional nanoscale metal network structure. (b) Variation of x_{Ag} with L in as-dealloyed samples after different dealloying times. Routes A and B refer to mild corrosion in 1 M $HClO_4$ and fast corrosion in 5 M HNO_3, respectively. Each data point represents an average over four samples produced simultaneously.

faster coarsening during prolonged corrosion. The scanning electron micrograph of Figure 1(a) illustrates the nanoscale network structure that is typical of as-dealloyed NPG (here route A), with a mean ligament size of 20 nm. EDS on a $20 \times 30\,\mu m^2$ area on a cleavage surface suggests the Ag atom fraction $x_{Ag} = 0.062$. Varying the duration of dealloying yields different values of x_{Ag} and L, as summarized in Figure 1(a). It is seen that route B provides for larger L and lesser x_{Ag}. Remarkably, the two routes show a consistent correlation of composition and ligament size, with x_{Ag} progressively decreasing as L increases.

Parts a–d in the left column of Figure 2 summarize our TEM characterization of a 30-nm-thick ultramicrotomy slice of as-dealloyed NPG with $L = 20$ nm. At the top is the HAADF image, showing that the characteristic NPG microstructure is conserved during cutting. EDS of the entire imaged region suggests a mean silver fraction $x_{Ag} = 0.055 \pm 0.003$, consistent with the data of Figure 1(b).

Figure 2(b–d) shows elemental maps of Ag and Au of the region in Figure 2(a), along with the overlay of both. The remarkable observation is that the structure is dominated by regions of (almost) pure Au, while most Ag is located in Ag-rich clusters. Local EDS quantification suggests $x_{Ag} = 0.0081 \pm 0.0008$ in the silver-depleted regions and the much higher $x_{Ag} = 0.50 \pm 0.06$ in the silver-rich regions. As regions may overlap, the true x_{Ag} in the clusters likely exceeds 0.5.

The right column of Figure 2 summarizes the TEM data of a 170-nm-thick slice of NPG which was coarsened to $L = 150$ nm by annealing for 30 min at 300 °C in air. The large L, along with the high atomic number of Au, entails considerable absorption for both, the electron beam and the x-rays. This absorption effect contributes to the contrast in the HAADF image. To minimize the error in EDS quantification due to absorbtion, Ag–K photons (22.16 keV) were used instead of the more familiar Ag–L ones (2.98 keV). The mean silver fraction emerged as $x_{Ag} = 0.052 \pm 0.003$. This agrees with the mean x_{Ag} in the as-dealloyed material, consistent with the notion that annealing leaves the Ag fraction invariant. The key observation is that the Ag distribution in the annealed sample appears homogeneous, in striking contrast to the clustering in the as-dealloyed sample.

Our study advertises three observations: First, during dealloying the net amount of residual Ag consistently decreases as the ligament size increases over time. Second, Ag is aggregated in discrete, three-dimensional regions or 'clusters'. Third, coarsening without corrosion—as in the annealing treatment—homogenizes the Ag distribution. We now argue that these observations are perfectly natural in view of the established atomic-scale mechanisms of dealloying, as they are implemented in our KMC approach.

Figure 3(a–d) illustrates our simulation results by means of snapshots after different times of dealloying at $T = 300$ K. Starting out from the planar surface of the master alloy (Figure 3(a)), corrosion roughens the surface while, at the same time, enriching the walls of the emerging pore channels in Au (Figure 3(b)). Bifurcation opens new channels, thereby establishing the characteristic microstructural length-scale of the network structure. In Figure 3(c), the corrosion has penetrated the entire

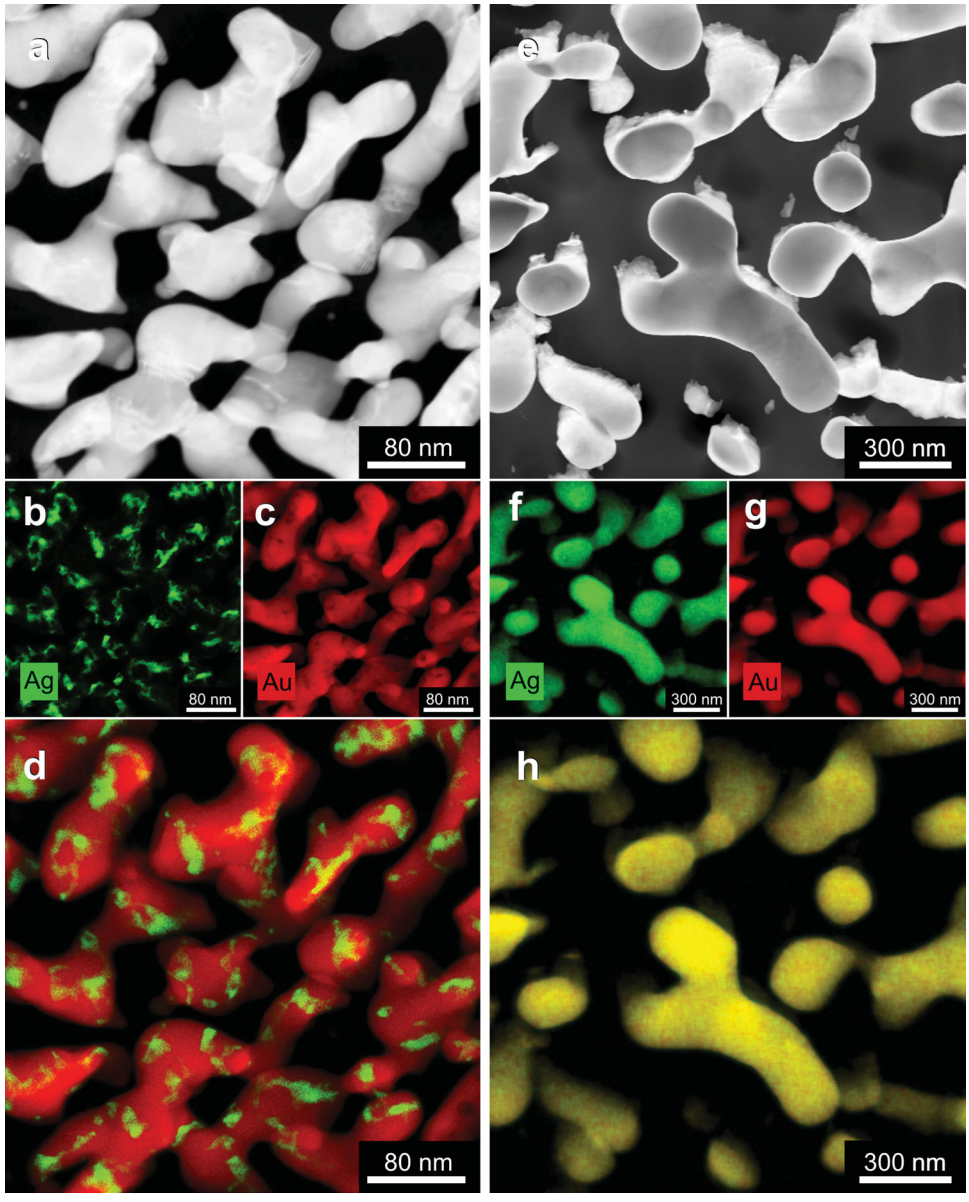

Figure 2. TEM of thin, microtome-cut slices of as-dealloyed (a–d) and annealed (e–h) NPG. (a, e) High-angle annular dark-field images illustrating the ligament size and geometry. (b, f) Element maps for Ag (green) and (c, g) Au (red). (d, h) Superimposed elemental maps of Ag and Au. (d) Clustering of Ag in the as-dealloyed state. (h) Uniform distribution of Ag in the annealed state. Note different scales for the respective states.

simulation box. The surfaces of this initial network tend to be covered (and passivated) by a single atomic monolayer of Au. Consequently, the interior of the ligaments is screened from corrosion and so retains the composition of the master alloy. Indeed, the net residual Ag fraction at this stage remains as high as 0.40.

Sustained exposure to corrosive conditions, as in typical dealloying experiments, leads to curvature-driven coarsening by surface diffusion. The coarsening can be perceived in Figure 3(d). Here, some of the original ligaments have been consumed, and aggregation of the Au on the surviving ligaments has increased the mean L by roughly 50%. The network now exhibits more extended regions of pure gold. As Ag that was exposed at the surface during coarsening has been dissolved, the net Ag fraction has decreased to 0.20. All residual silver is located in relics of the original master alloy that have not yet been exposed to corrosion. The local silver fraction in those regions remains that of the master alloy.

The mean ligament size of NPG increases with time, t, as $t^{1/4}$ [38,39], and eventually the growth will be so slow that the mean structure size can be considered stationary for practical purposes; it is this state of the material that is investigated in many experimental studies of

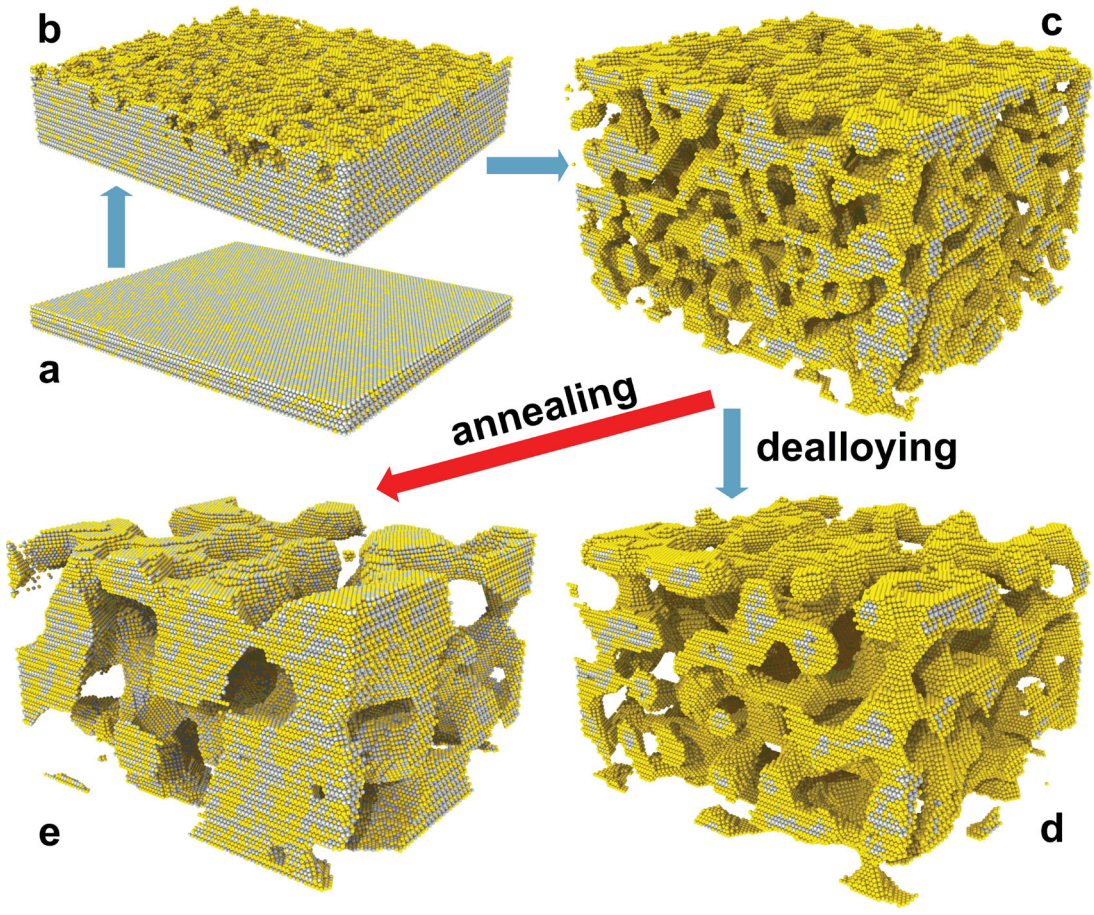

Figure 3. Microstructure evolution during dealloying and coarsening from KMC simulation. Au atoms yellow, Ag atoms gray. (a) Original master alloy surface. Snapshots after 8×10^5 KMC steps ($\sim$ 2.7 s laboratory time, (b)), 8×10^6 steps ($\sim$ 27 s, (c)) and 2×10^8 steps ($\sim$ 300 s, (d)) of corrosion at 300 K show formation and coarsening of nanoscale network structure. Note localization of Ag in relics of not-corroded master alloy. Microstructure in (e) was generated by annealing the structure from (c) at 675 K for 5×10^8 steps ($\sim$ 0.12 ms). Note the more homogeneous Ag distribution.

NPG as structural or functional material. Even though our simulation did not reach the time frame required for coarsening to a realistic ligament size, comparing the simulated structure in Figure 3(d) to the TEM images in Figure 2(a–d) reveals close agreement in microstructural geometry. Most significantly, both approaches show the heterogeneous distribution of Ag.

Figure 4(a) shows a tomographic reconstruction of the as-dealloyed material, based on EDS data. The 3D representation strikingly illustrates the Ag-rich clusters embedded in Au-rich ligaments. Comparison of slices cut from experimental reconstruction (Figure 4(b)) and simulation (Figure 4(c)) further emphasizes the agreement between the two approaches. The TEM data of Figure 4 suggest that some Ag clusters may be connected to the surface. Yet, with a voxel size of 1.5 nm^3, the reconstruction would not resolve the Au-rich superficial atomic monolayers that isolate the clusters from the surface in the simulation. As these layers are required for passivating the surface and conserving the clusters, the combination of experiment and simulation points strongly towards their presence.

With an eye on the experimental results for the annealed samples, we have also simulated annealing via KMC. Starting with the structure of Figure 3(c), Ag dissolution was switched off and the simulation run at $T =$ 675 K until L had roughly doubled. Figure 3(e) shows that Ag is now almost uniformly distributed throughout the entire solid, and specifically Ag atoms are now also found at the surface. Thus, the simulation and the elemental map of Figure 2(h) independently confirm that annealing homogenizes the silver distribution in NPG. Note that the simulation here considers surface diffusion as the only active mechanism.

The neglect of bulk diffusion in our discussion is of relevance, since that process would (A) homogenize the alloy and (B) promote Ag dissolution independent of coarsening, in conflict with our observations of Ag clustering and of a correlation between x_{Ag} and L. Bulk diffusion can be a relevant process in dealloying at

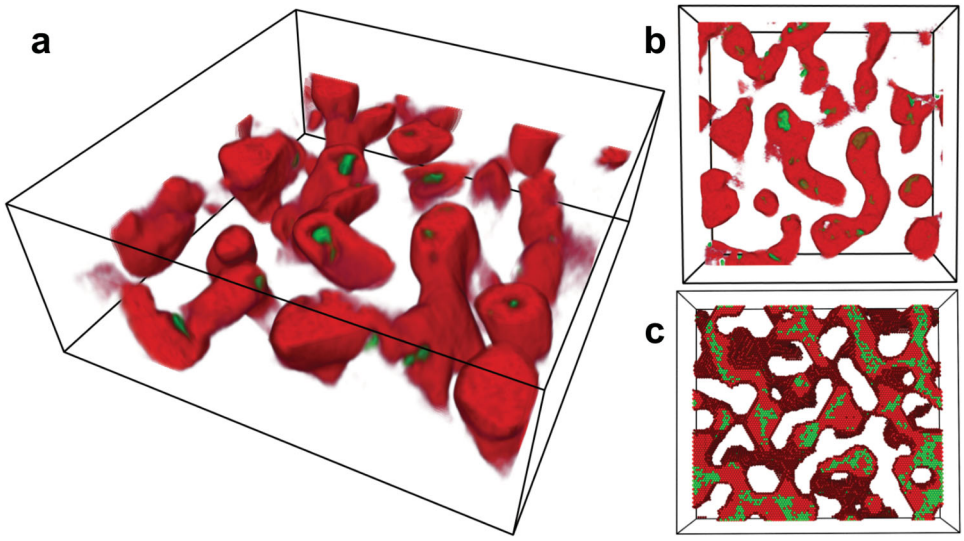

Figure 4. Three-dimensional representation of silver distribution. (a) Experiment; reconstruction based on spectrum image tilt series of a 70-nm-thick slice of as-dealloyed NPG. Gold-rich areas from principal component analysis colored red, silver-rich areas green. (b) 5-nm thin slab extracted from the reconstruction in (a). (c) Comparison to simulation: Slab of 5 atom layers from the microstructure of Figure 3d. In (c), Au atoms are red, dark red for surface atoms, Ag atoms green. Box edge lengths are 500 nm in (b), 25 nm in (c). Note consistent geometries in experiment and simulation, with aggregation of Ag in clusters.

high homologous temperature [40]. Yet, for Ag–Au near room temperature conventional bulk diffusion is so much slower than surface diffusion that any significant contribution to microstructure evolution can, indeed, be ruled out [40,41]. In their discussion of the shrinkage of NPG at high dealloying potentials, Jin and coworkers advertise the possibility of vacancy injection at the corrosion front and the role of its consequence, accelerated bulk diffusion, for dealloying [42]. Our simulation disregards bulk diffusion and so does not explore this mechanism. Yet, the agreement of the simulation results with our TEM observations supports surface diffusion as the controlling transport mechanism under the conditions of the present experiment.

The homogenization of the Ag distribution by ex situ coarsening has been confirmed before [11]. A silver-rich surface segregation layer might also be formed, particularly during coarsening in air, since oxygen binds more strongly to Ag than to Au, thereby promoting Ag enrichment at the surface. The resolution of our TEM data is insufficient for discussing the local Ag fraction in the surface atomic layers. Yet, in as much as as-prepared NPG—that is, the NPG with small ligament size which is the object of most studies in the field—is concerned, our study suggests that the major part of the net Ag fraction is buried in clusters and is thus not available for influencing the chemistry at the surface. Furthermore, our simulation confirms that the corrosive environment during dealloying removes essentially all Ag from the surface. Claims of a decisive role of Ag for the catalytic activity might need to be reconsidered from that perspective. Similarly, if Ag is enriched in clusters it follows that most regions of the bulk crystal lattice contain substantially lesser Ag than suggested by the net Ag fraction. This implies that the effect of Ag in reducing the stacking fault energy in Au is not exploited. Studies of dislocation plasticity of NPG may, therefore, need to consider the comparatively high stacking fault energy of pure Au, not the reduced value in the alloy.

Our results support and illustrate the notion, advertised in [42], of dealloying as a two-stage process. The *primary* dealloying establishes a 3D porous structure, in which the ligaments are passivated by Au-rich layers while their core retains the composition of the master alloy. This state, which is illustrated by our Figure 3(c), retains a high residual Ag fraction. Under the conditions of our study, coarsening behind the corrosion front goes along with further removal of Ag and with the growth of Au-rich regions. This process exemplifies *secondary* dealloying and leads to structures such as our Figure 4. Interestingly, the size of the surviving Ag-rich clusters, which are revealed in our study, provides a signature of the structure size established during the *primary* dealloying. This initial structure size is relevant for our understanding of the mechanisms of dealloying, yet it is difficult to observe by other means. Systematic studies of silver clusters sizes formed under different corrosion conditions might thus be an interesting subject for future experiments.

Disclosure statement

No potential conflict of interest was reported by the authors.

Funding

This work was supported by Deutsche Forschungsgemeinschaft (DFG) through SFB986 'M^3', subprojects B2 and Z3 and through FOR2213 'NAGOCAT', subproject 3.

ORCID

Jörg Weissmüller http://orcid.org/0000-0002-8958-4414

References

[1] Erlebacher J, Aziz MJ, Karma A, et al. Evolution of nanoporosity in dealloying. Nature. 2001;410(6827):450–453.
[2] Biener J, Hodge AM, Hamza AV, et al. Nanoporous Au: a high yield strength material. J Appl Phys. 2005;97(2):024301.
[3] Volkert CA, Lilleodden ET, Kramer D, et al. Approaching the theoretical strength in nanoporous Au. Appl Phys Lett. 2006;89(6):061920-061920-3.
[4] Hodge AM, Biener J, Hayes JR, et al. Scaling equation for yield strength of nanoporous open-cell foams. Acta Mater. 2007;55(4):1343–1349.
[5] Jin HJ, Kurmanaeva L, Schmauch J, et al. Deforming nanoporous metal. Role of lattice coherency. Acta Mater. 2009;57(9):2665–2672.
[6] Jin HJ, Weissmüller J. A material with electrically tunable strength and flow stress. Science. 2011;332(6034):1179–1182.
[7] Briot NJ, Kennerknecht T, Eberl C, et al. Mechanical properties of bulk single crystalline nanoporous gold investigated by millimetre-scale tension and compression testing. Philos Mag. 2014;94(8):847–866.
[8] Sun S, Chen X, Badwe N, et al. Potential-dependent dynamic fracture of nanoporous gold. Nat Mater. 2015;14(9):894–898.
[9] Mameka N, Wang K, Markmann J, et al. Nanoporous gold-testing macro-scale samples to probe small-scale mechanical behavior. Mater Res Lett. 2016;4(1):27–36.
[10] Kramer D, Viswanath RN, Weissmüller J. Surface-stress induced macroscopic bending of nanoporous gold cantilevers. Nano Lett. 2004;4(5):793–796.
[11] Zhang L, Chen L, Liu H, et al. Effect of residual silver on surface-enhanced raman scattering of dealloyed nanoporous gold. J Phys Chem C. 2011;115(40):19583–19587.
[12] Detsi E, Chen ZG, Vellinga WP, et al. Actuating and sensing properties of nanoporous gold. J Nanosci Nanotechnol. 2012;12(6):4951–4955.
[13] Stenner C, Shao LH, Mameka N, Piezoelectric gold, et al. Strong charge-load response in a metal-based hybrid nanomaterial. Adv Funct Mater. 2016;26(28):5174–5181.
[14] Ye XL, Liu LZ, Jin HJ. Responsive nanoporous metals: recoverable modulations on strength and shape by watering. Nanotechnology. 2016;27(32):325501.
[15] Lang XY, Yuan HT, Iwasa Y, et al. Three-dimensional nanoporous gold for electrochemical supercapacitors. Scripta Mater. 2011;64(9):923–926.
[16] Ding Y, Chen MW. Nanoporous metals for catalytic and optical applications. MRS Bull. 2009;34:569–576.
[17] Lang X, Qian L, Guan P, et al. Localized surface plasmon resonance of nanoporous gold. Appl Phys Lett. 2011;98(9):093701.
[18] Jalas D, Canchi R, Petrov AY, et al. Effective medium model for the spectral properties of nanoporous gold in the visible. Appl Phys Lett. 2014;105(24):241906.
[19] Xue Y, Markmann J, Duan H, et al. Switchable imbibition in nanoporous gold. Nature Commun. 2014;5:4237.
[20] Zielasek V, Jürgens B, Schulz C, et al. Gold catalysts: nanoporous gold foams. Angew Chem Int Ed. 2006;45(48):8241–8244.
[21] Xu C, Su J, Xu X, et al. Low temperature co oxidation over unsupported nanoporous gold. J Amer Chem Soc. 2007;129(1):42–43.
[22] Erlebacher J. An atomistic description of dealloying – porosity evolution, the critical potential, and rate-limiting behavior. J Electrochem Soc. 2004;151(10):C614–C626.
[23] Hodge AM, Doucette RT, Biener MM, et al. Ag effects on the elastic modulus values of nanoporous Au foams. J Mater Res. 2009;24(4):1600–1606.
[24] Greer JR, Oliver WC, Nix WD. Size dependence of mechanical properties of gold at the micron scale in the absence of strain gradients. Acta Mater. 2005;53(6):1821–1830.
[25] Greer JR, Nix WD. Nanoscale gold pillars strengthened through dislocation starvation. Phys Rev B. 2006;73(24):245410.
[26] Huber N, Viswanath RN, Mameka N, et al. Scaling laws of nanoporous metals under uniaxial compression. Acta Mater. 2014;67(0):252–265.
[27] Ngô BND, Stukowski A, Mameka N, et al. Anomalous compliance and early yielding of nanoporous gold. Acta Mater. 2015;93(0):144–155.
[28] Wittstock A, Wichmann A, Biener J, et al. Nanoporous gold: a new gold catalyst with tunable properties. Faraday Discuss. 2011;152:87–98.
[29] Moskaleva LV, Röhe S, Wittstock A, et al. Silver residues as a possible key to a remarkable oxidative catalytic activity of nanoporous gold. Phys Chem Chem Phys. 2011;13(10):4529–4539.
[30] Wang LC, Zhong Y, Widmann D, et al. On the role of residual ag in nanoporous au catalysts for co oxidation: a combined microreactor and tap reactor study. ChemCatChem. 2012;4(2):251–259.
[31] Fujita T, Guan P, McKenna K, et al. Atomic origins of the high catalytic activity of nanoporous gold. Nature Mater. 2012;11(9):775–780.
[32] Rohe S, Frank K, Schaefer A, et al. Co oxidation on nanoporous gold: a combined TPD and XPS study of active catalysts. Surf Sci. 2013;609:106–112.
[33] Li D, Zhu Y, Wang H, et al. Nanoporous gold as an active low temperature catalyst toward CO oxidation in hydrogen-rich stream. Sci Rep. 2013;3(3015):1–7.
[34] Wang K, Kobler A, Kübel C, et al. Nanoporous-gold-based composites: toward tensile ductility. NPG Asia Mater. 2015;7(6):e187.

[35] de la Pea F, Ostasevicius T, Fauske VT, et al. hyperspy: Hyperspy 1.1; 2016 August. https://protect-us.mimecast.com/s/mmgYBRsOlbMvSY?domain=dx.doi.org.
[36] Al-Futaisi A, Patzek TW. Extension of hoshen-kopelman algorithm to non-lattice environments. Phys A: Stat Mech Appl. 2003;321(3–4):665–678.
[37] Stukowski A. Visualization and analysis of atomistic simulation data with OVITO - the Open Visualization Tool. Model Simul Mater Sci Eng. 2010;18(1):015012. http://ovito.org.
[38] Sieradzki K, Corderman RR, Shukla K, et al. Computer simulations of corrosion: Selective dissolution of binary alloys. Philos Mag A. 1989;59(4):713–746.
[39] Dursun A, Pugh D, Corcoran S. Dealloying of Ag-Au Alloys in Halide-Containing Electrolytes. J Electrochem Soc. 2003;150(7):B355–B360.
[40] Chen Q, Sieradzki K. Spontaneous evolution of bicontinuous nanostructures in dealloyed li-based systems. Nat Mater. 2013;12(12):1102–6.
[41] Schofield E. Anodic routes to nanoporous materials. Trans Inst Metal Finish. 2005;83(1):35–42.
[42] Ye XL, Lu N, Li XJ, et al. Primary and secondary dealloying of Au(Pt)–Ag: Structural and compositional evolutions, and volume shrinkage. J Electrochem Soc. 2014;161(12):C517–C526.